JOURNAL OF THERMOPHYSICS AND HEAT TRANSFER
Vol. 15, No. 2, April–June 2001

Heat Transfer Predictions Using a Dual-Dissipation k–ε Turbulence Closure

U. Goldberg* and P. Batten†
Metacomp Technologies, Inc., Westlake Village, California 91361

Wall heat transfer predictions, under both low- and high-speed separated flow conditions, are considered using a linear k–ε–R model and a cubic k–ε turbulence closure. The three-equation model is observed not to suffer the impediment of traditional k–ε models of severely overpredicting heat transfer in strongly out-of-equilibrium flow regions. This improvement is due to a dual-dissipation approach in which the destruction term in the k transport equation (based on a pseudoeddy-viscosity variable R) is independent of the length-scale-determining dissipation ε near walls. As a result, turbulence generation level is kept within reasonable bounds in nonequilibrium flow regions. Three flow cases involving wall heat transfer are considered: one in the low-speed regime and the others in the hypersonic regime. The advantage of the k–ε–R model is clearly demonstrated in the high-speed flow cases.

Nomenclature

A_E	=	constant in Eq. (11)
A_μ	=	constant in Eq. (14)
C_f	=	skin-friction coefficient
C_p	=	specific heat at constant pressure
C_{R1}, C_{R2}	=	constants in Eq. (5)
$C_{\varepsilon 1}$, $C_{\varepsilon 2}$	=	constants in Eq. (4)
C_μ	=	0.09 [Eq. (2)]
E	=	term in the ε transport equation [see Eq. (11)]
f_d	=	term in the R transport equation [see Eq. (13)]
f_μ	=	low Reynolds damping function [see Eq. (14)]
H	=	step height
k	=	turbulence kinetic energy
M	=	Mach number
P_k	=	turbulence production [see Eq. (6)]
Pr	=	Prandtl number
q	=	heat transfer rate
R	=	pseudoeddy viscosity
Re	=	Reynolds number
R_t	=	turbulence Reynolds number
T	=	timescale, temperature (context dependent)
t	=	time
U	=	mean velocity
U_t	=	tangential velocity component
$\overline{u_i u_j}$	=	Reynolds stress tensor
u_τ	=	friction velocity, $(\tau/\rho)_w^{1/2}$
$\mathcal{V}$	=	realizable velocity scale [see Eq. (10)]
x	=	streamwise coordinate (without subscript)
y	=	local wall-normal coordinate
y^+	=	inner-layer nondimensional coordinate, yu_τ/ν_w
δ	=	boundary-layer thickness
δ_{ij}	=	3 if $i = j$, 0 otherwise (summation assumed)
ε	=	turbulence kinetic energy dissipation rate
κ	=	0.41 (von Kármán constant)
μ	=	dynamic viscosity
ν	=	kinematic viscosity, μ/ρ
Π	=	wake strength parameter
ρ	=	density
σ_k, σ_ε, σ_R	=	turbulent diffusion coefficients
τ	=	turbulence timescale, shear stress (context dependent)
Ψ	=	component of the source term E [see Eq. (9)]
∇	=	gradient operator

Subscripts

i or j	=	Cartesian component in the i or j direction
i, j	=	j-direction derivative of the i component
t	=	turbulent
w	=	evaluated at the wall
x	=	based on streamwise direction
0	=	stagnation conditions
1	=	wall-adjacent cell centroid
∞	=	evaluated at the freestream

Received 25 July 2000; revision received 9 October 2000; accepted for publication 11 October 2000.

*Senior Scientist, 650 Hampshire Road, No. 200.
†Scientist, 650 Hampshire Road, No. 200.

Introduction

CONVENTIONAL k–ε models are notorious for severely overpredicting heat transfer levels in flows involving strong enough adverse pressure gradient to cause separation, as documented in detail by Launder.[1] This stems from ill-understood deficiencies in the ε transport equation in nonequilibrium near-wall regions, which can lead to excessive levels of the length scale generated in separated flows and, hence, to correspondingly excessive heat transfer levels, especially in the reattachment region. Modifications to the ε equation were successful in improving heat transfer predictions under low-speed conditions,[1] but failed in high-speed flow.

Most, if not all, modern turbulence closures have been derived and calibrated with reference to incompressible or low-speed fluid flow in which compressibility effects are unimportant. The well-known overprediction of heat transfer in nonequilibrium conditions using conventional k–ϵ closures has several possible (and ill-understood) origins. Clearly, at high Mach numbers, models will be pushed further from their (typically equilibrium) calibration range due to the increasing mean shear stress. Increased anisotropy should be expected in higher Mach number flows, due to the restriction of spatial correlations caused by the narrowing cone of influence. Another significant factor is that of the mean density gradients. Huang et al.[2] have demonstrated that the choice of length-scale-determining variable has a strong effect on the ability of the model to predict the compressible (van Driest) law of the wall, with k–ϵ displaying particularly poor behavior, but with no existing model performing well. The density fluctuations and the nondivergent nature of the velocity field are further potentially influential features. These have led to recent proposals for dilatational dissipation models that, although give the correct trend for free-shear flows, tend to worsen predictions in the near-wall region.[2] Against this background of physical and modeling uncertainties, no existing turbulence closure has been found to perform adequately.

One possible approach to improving the performance of k–ε type models is presented here. Whereas a conventional dissipation-rate equation is used to determine the large-eddy length scale for the eddy-viscosity field, $\nu_t \sim k^{1/2}(k^{3/2}/\varepsilon)$, an additional transport equation is used to determine a second dissipation rate, $\hat{\varepsilon} = k^2/R$, defining the destruction term in the k equation. This term is independent of ε in the immediate vicinity of walls and yields a more faithful representation of near-wall eddy-dissipation rates. The resulting effect is to avoid excessive imbalance between the generation and destruction of k in nonequilibrium flow regions, leading to reasonable turbulence generation levels and, hence, reasonable heat transfer predictions. The improvement in high-speed flows is shown to be quite dramatic.

Highlights of the Numerical Approach

CFD++, a Navier–Stokes flow solver for either compressible or incompressible fluid flows, was used here. This code features a second order total variation diminishing discretization based on a multidimensional interpolation framework. For the results presented here, a Harten–Lax–van Leer, with contact wave (HLLC) Riemann solver was used to define the (limited) upwind fluxes. The HLLC Riemann solver is particularly suitable for hypersonic flow applications because, unlike classical linear solvers such as Roe's scheme, it automatically enforces entropy and positivity conditions. Further details on the numerical methodology in CFD++ may be found in Refs. 3–6.

k–ε–R Turbulence Model Formulation

In this model, a variant of the one described in Ref. 7, Reynolds stresses are related to the mean strain through the Boussinesq approximation:

$$-\rho\overline{u_i u_j} = \mu_t\left(U_{i,j} + U_{j,i} - \tfrac{2}{3}U_{k,k}\delta_{ij}\right) - \tfrac{2}{3}\rho k\delta_{ij} \tag{1}$$

where the eddy-viscosity field is given by

$$\mu_t = C_\mu f_\mu \rho k^2/\varepsilon \tag{2}$$

where f_μ is a damping function discussed later. The turbulence kinetic energy k, the conventional dissipation rate ε, and the pseudoeddy viscosity R, respectively, are determined by the following transport equations:

$$\frac{\partial(\rho k)}{\partial t} + \frac{\partial}{\partial x_j}(U_j\rho k) = \frac{\partial}{\partial x_j}\left[\left(\mu + \frac{\mu_t}{\sigma_k}\right)\frac{\partial k}{\partial x_j}\right] + P_k - \rho\hat{\varepsilon} \tag{3}$$

$$\frac{\partial(\rho\varepsilon)}{\partial t} + \frac{\partial}{\partial x_j}(U_j\rho\varepsilon) = \frac{\partial}{\partial x_j}\left[\left(\mu + \frac{\mu_t}{\sigma_\varepsilon}\right)\frac{\partial \varepsilon}{\partial x_j}\right] + (C_{\varepsilon 1}P_k - C_{\varepsilon 2}\rho\varepsilon + E)T_t^{-1} \tag{4}$$

$$\frac{\partial(\rho R)}{\partial t} + \frac{\partial}{\partial x_j}(U_j\rho R) = \frac{\partial}{\partial x_j}\left[\left(\mu + \frac{\mu_t}{\sigma_R}\right)\frac{\partial R}{\partial x_j}\right] + (2 - C_{R1})P_k\frac{R}{k} - (2 - C_{R2})\rho k - (1 + f_d)\rho\frac{C_\mu}{\sigma_R}\frac{\partial R}{\partial x_j}\frac{\partial R}{\partial x_j} \tag{5}$$

P_k is the turbulence production, $-\rho\overline{u_i u_j}U_{i,j}$, which, when modeled in terms of the Boussinesq concept in Eq. (1), reduces to

$$P_k = \left[\mu_t\left(\frac{\partial U_i}{\partial x_j} + \frac{\partial U_j}{\partial x_i} - \frac{2}{3}\frac{\partial U_k}{\partial x_k}\delta_{ij}\right) - \frac{2}{3}\rho k\delta_{ij}\right]\frac{\partial U_i}{\partial x_j} \tag{6}$$

Here U_i are the Cartesian mean velocity components, x_i are the corresponding coordinates, and μ and μ_t are the molecular and eddy viscosities, respectively. The constants appearing in these transport equations are given later.

In Eq. (3), a second dissipation rate is defined, given by

$$\hat{\varepsilon} = k^2/R \tag{7}$$

The following realizable timescale is used in Eq. (4):

$$T_t = (k/\varepsilon)\max\{1, \xi\} \tag{8}$$

where $\xi = C_\tau/\sqrt{R_t}$, where $R_t = \rho k^2/(\mu\varepsilon)$ is the turbulence Reynolds number and C_τ is a constant given subsequently. This timescale is k/ε at large R_t (hence, small ξ) but becomes proportional to the Kolmogorov scale, $C_\tau\sqrt{(\nu/\varepsilon)}$, for $R_t \ll 1$. Note that including T_t in the ε equation guarantees near-wall asymptotic consistency of that equation without resorting to ad hoc damping functions found in many k–ε models.

The extra source term E in Eq. (4) is designed to increase the level of ε in nonequilibrium flow regions, thereby reducing the length scale and enabling improved prediction of adverse pressure gradient flows:

$$\Psi = \max\left\{\frac{\partial k}{\partial x_j}\frac{\partial \tau}{\partial x_j}, 0\right\} \tag{9}$$

$$\mathcal{V} = \max\left\{k^{\frac{1}{2}}, (\nu\varepsilon)^{\frac{1}{4}}\right\} \tag{10}$$

$$E = A_E\rho\mathcal{V}\sqrt{\varepsilon T_t}\Psi \tag{11}$$

where $\tau = k/\varepsilon$ is the turbulence timescale. The extra source term is invoked only in near-wall regions, where $\Psi > 0$, increasing ε and thereby decreasing the length scale. Note the realizable velocity scale $\mathcal{V}$ used here. Its presence limits the region of influence of E to a relatively small fraction of the boundary layer near walls, with a sharp cutoff farther away.

The transport equation for R includes the function f_d, determined as follows:

$$\varphi = \frac{\partial R}{\partial x_j}\frac{\partial(R/k)}{\partial x_j} \tag{12}$$

$$f_d = \frac{\varphi}{|\varphi|} \tag{13}$$

Thus, the second destruction term in the R equation is invoked only in near-wall portions of boundary layers, where $\varphi > 0$. Note that R/k and k/ε define two distinct turbulence timescales.

The damping function f_μ is based on the following: In near-wall regions the proper velocity scale[8] is $\sqrt{v^2}$, not $\sqrt{k}$, and the timescale is the realizable one, Eq. (8). The form currently adopted is[9]

$$f_\mu = \frac{1 - e^{-A_\mu R_t}}{1 - e^{-\sqrt{R_t}}}\max\{1\ ,\ \xi\} \tag{14}$$

where A_μ is a constant to be given. Note that $f_\mu \to A_\mu C_\tau$ as $R_t \to 0$. This type of near-wall limit was also adopted by Durbin,[8] who argued that $\mu_t \sim y^4$, rather than y^3, is acceptable since $\mu_t \ll \mu$ there.

Finally, the model constants are $C_\mu = 0.09$, $C_{\varepsilon 1} = 1.44$, $C_{\varepsilon 2} = 1.92$, $C_{R1} = 1.4$, $C_{R2} = 1.8$, $\sigma_k = \sigma_R = C_\mu^{1/2}\kappa^2(C_\mu^{-1} - 2)/(C_{R2} - C_{R1}) = 1.15$, $\sigma_\varepsilon = 1.3$, $C_\tau = \sqrt{2}$, $A_\mu = 0.016$, and $A_E = 0.3$. The first three constants and σ_ε are standard, the R equation constants are determined from asymptotic consistency at the logarithmic overlap, C_τ is determined from the behavior of k in the viscous sublayer, and the last two constants are set through forcing correct prediction of the log-law constant ($\approx$5.2) in near-wall flat plate and channel flows.

The three transport equations are subject to the following boundary conditions at solid walls. The kinetic energy of turbulence and its first normal-to-wall derivative vanish there. The former condition is implemented directly:

$$k_w = 0 \tag{15}$$

The boundary condition for ε is commonly given as $\varepsilon_w = 2[\nu(\partial\sqrt{k}/\partial y)^2]_w$. However, due to the partially decoupled nature of k and ε, this may no longer hold true and a Neumann condition was used here as an alternative:

$$\left(\frac{\partial \varepsilon}{\partial y}\right)_w = 0 \tag{16}$$

Last, the boundary condition for R ($\equiv k^2/\hat{\varepsilon}$) is

$$R_w = 0 \tag{17}$$

The effect of the turbulence destruction term $\hat{\varepsilon}$ in the k equation is best understood from realizing that ε affects the transport of R only through turbulent diffusion and generation. In the viscous sublayer, both are negligible since $\mu_t \ll \mu$ and Eq. (5) reduces to

$$\nu \frac{d^2 R}{dy^2} = (2 - C_{R2})k \tag{18}$$

This leads to

$$\hat{\varepsilon} = \frac{k^2}{R} \approx \frac{2\nu}{2 - C_{R2}} \frac{1}{k} \frac{d}{dy}\left(k \frac{dk}{dy}\right) \tag{19}$$

Thus, the sink term in the k equation is a function of k and its derivatives and is independent of ε in the immediate proximity of walls. This prevents the predicted level of turbulence generation from soaring near walls even in strongly nonequilibrated flow regions. In contrast, the forcing term in a standard k–ε model, $P_k - \varepsilon$, can become very large in such regions, leading to correspondingly large turbulence generation levels.

Results

In the following flow test cases, the linear k–ε–R model's performance is compared with experimental data as well as with predictions by a cubic k–ε closure,[9] also topography-parameter free. Whereas the latter accounts for both Reynolds stress anisotropy and streamline curvature (including swirl effects), it does not possess any modifications designed for improved heat transfer prediction. Before addressing this issue, two basic test cases are used to ascertain the high fidelity of both models: subsonic flow over a flat plate and transonic flow in a channel with a bump on one wall. These are followed by three cases involving heat transfer: a low-speed flow, a two-dimensional hypersonic flow, and a three-dimensional hypersonic flow. Heat fluxes were modeled as

$$\nabla q = -C_p(\mu/Pr + \mu_t/Pr_t)\nabla T \tag{20}$$

where q is the heat transfer rate, C_p is the specific heat at constant pressure, $Pr = 0.72$ and $Pr_t = 0.9$ are the molecular and turbulence Prandtl numbers, respectively, and T is temperature. Sutherland's law was used to model the variation of molecular viscosity with temperature.

Flow Over a Flat Plate

Mach 0.2 flow over an adiabatic flat plate at Reynolds number of 6×10^6 is computed on a 65×97 grid, with $y^+ \leq 1$ at the first centroidal location away from the wall. The plate's leading edge is preceded by a section of freestream flow parallel to it. Figure 1a shows skin-friction distribution compared to the correlation $C_f \approx 0.455/(\ln^2 0.06 Re_x)$ (Ref. 10). In this test case, the Spalart–Allmaras (S–A) closure[11] was also invoked. The skin-friction profiles predicted by the three-equation and the S–A models are similar and slightly underpredict the correlation, whereas the cubic closure's prediction is in close agreement with it. Figure 1b shows profiles of streamwise velocity at $x = 0.84$ m. The boundary-layer thickness predicted by all models is close to 0.015 m, in agreement with the correlation $\delta/x = 0.37/Re_x^{1/5}$ (Ref. 10). Figure 2 compares the two turbulence energy dissipation rates used in the three-equation model, namely, ε and $\hat{\varepsilon}$, with ε from the cubic model. It is observed that under near-equilibrium conditions the three dissipation rates are in close agreement.

Transonic Channel Flow Including Bump

In this case, a Mach 0.615 flow enters a two-dimensional channel comprising a flat upper wall and a lower surface that includes a bumplike profile protruding from the otherwise flat wall (Fig. 3). The inflow total pressure is 96 kPa. A transonic λ shock forms toward the bump trailing edge (Fig. 3), and its interaction with the boundary

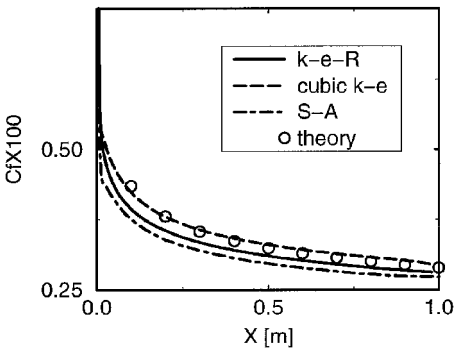

a) Skin friction

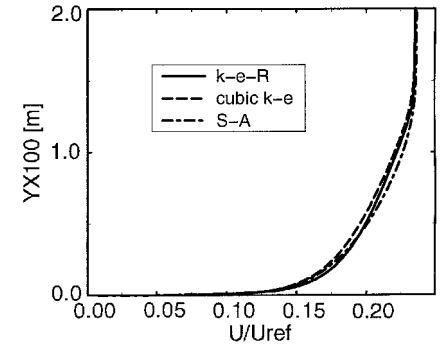

b) Streamwise velocity profiles at $x = 0.84$ m; $M = 0.2$

Fig. 1 Flat plate.

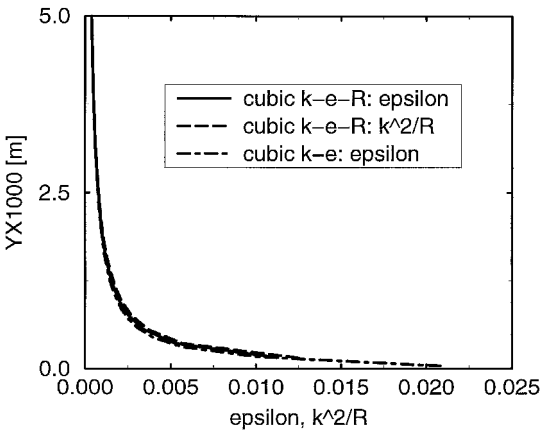

Fig. 2 Flat plate: turbulence dissipation rates in the three-equation model; $x = 0.84$ m, $M = 0.2$.

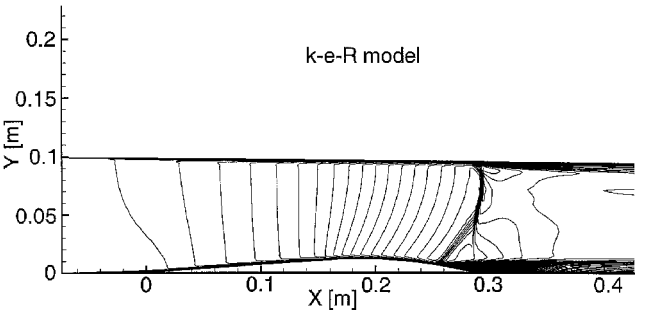

Fig. 3 Délery bump: topography and streamwise velocity contours.

layer induces a separated flow region. Experimental data were taken by Délery.[12] In the experiment, the shock location was controlled by an adjustable throat downstream of the bump. Because no geometrical details of this throat are provided, it is customary to adjust the downstream pressure to approximate numerically the experimental shock location on the upper wall. In the present calculations $p/p_\infty = 0.82$ was imposed. Adiabatic, nonslip conditions were imposed at the walls, and the inflow boundary was set to reservoir

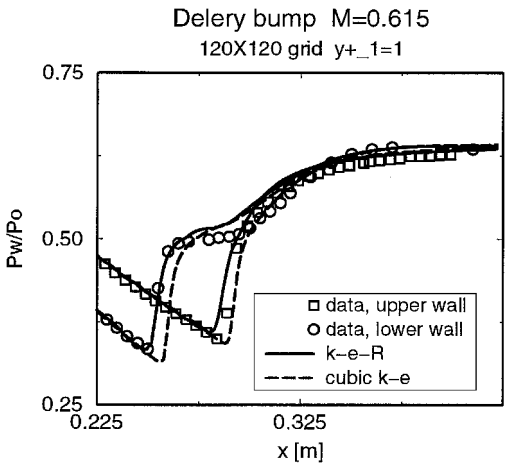

a) Wall pressure profiles

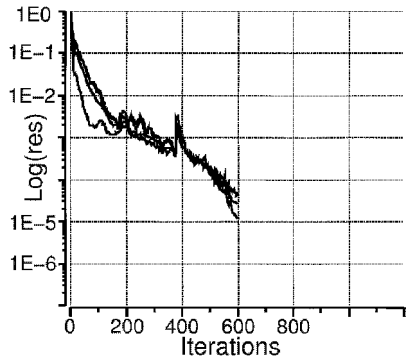

b) Convergence history

Fig. 4 Délery bump.

conditions. The computations were done on two grids: a 120×120 grid with 14 points inside the viscous sublayers, with the first point located at $y^+ = 0.1$, and a 120×240 grid, with 16 points inside the sublayers and finer resolution across the channel. The latter established grid independence of the former mesh. The computational domain extended from $x = -74$ to $x = 426$ mm. Some streamwise grid clustering was imposed, centered at the bump trailing edge. Figure 4a shows comparisons of predictions with experimental data of upper and lower wall pressure profiles. These results indicate that the two models capture the shock location and postshock behavior correctly. Figure 4b is a convergence history plot, based on mass, momentum, and energy residuals, which dropped four orders of magnitude in 500 steps.

Heat Transfer Downstream of an Abrupt Circular Tube Expansion

Baughn et al.[13] performed flow measurements in a sudden expansion between two circular tubes. Flow conditions were $M_\infty = 0.0078$, $Re_D = 1.73 \times 10^4$ (based on the larger tube diameter) and $T_\infty = 288$ K. The 2-m-long upstream tube was insulated while the downstream one was kept at a uniform wall temperature $T_w = 298$ K. Figure 5a shows the geometry and main flow features, in particular the recirculation region downstream of the expansion. The pipe boundary layer was allowed to develop from constant inflow conditions. Calculations on 13,000 and 21,000 mesh sizes, both with $y_1^+ = 1$, yielded only slight changes, and the reported predictions are based on the larger grid. Figure 5b shows the calculation's convergence history. A residual drop by three orders of magnitude was reached in 300 steps. Figure 6 shows comparisons of predictions with experimental data of wall heat transfer (Fig. 6a) and centerline velocity (Fig. 6b) and Fig. 7 shows velocity and temperature profiles (Figs. 7a and 7b, respectively), each at $x/H = 1.0$ and 10.0. The cubic model slightly overpredicts the wall heat transfer, whereas the three-equation closure underpredicts the peak level correctly. The latter model also predicts the centerline velocity slightly better than

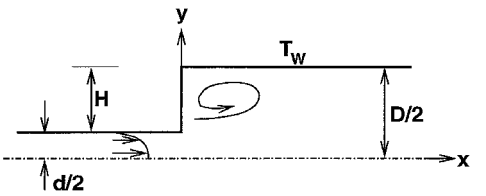

a) Topography and main flow features, $d = 3.81$ cm, $D = 2.5d$, $H = 0.75d$, and $M = 0.0078$

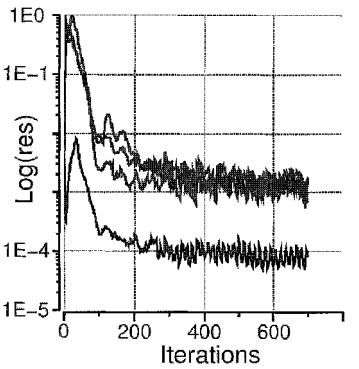

b) Solution convergence history

Fig. 5 Sudden expansion.

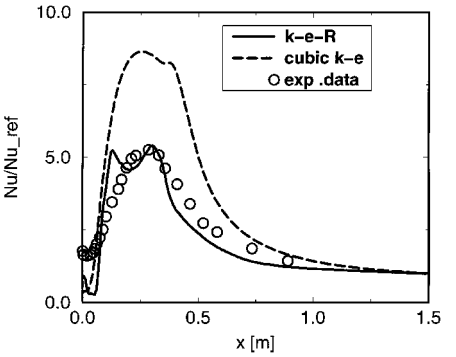

a) Wall heat transfer

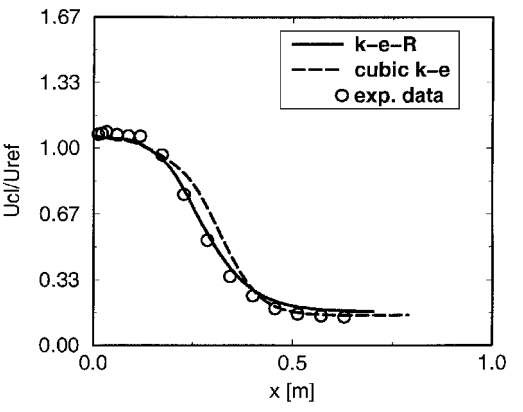

b) Centerline velocity

Fig. 6 Sudden expansion.

does the cubic model. Both closures seem to overpredict the extent of the separation bubble, but the three-equation model predicts the velocity profile at $x/H = 10$ somewhat better. The temperature profiles are not very well predicted by either model, but here the cubic closure has a slight advantage.

Hypersonic Flow over a Compression Ramp

This case is a two-dimensional Mach 9 flow over a 38-deg cooled ramp, with experimental data measured by Coleman and Stollery.[14]

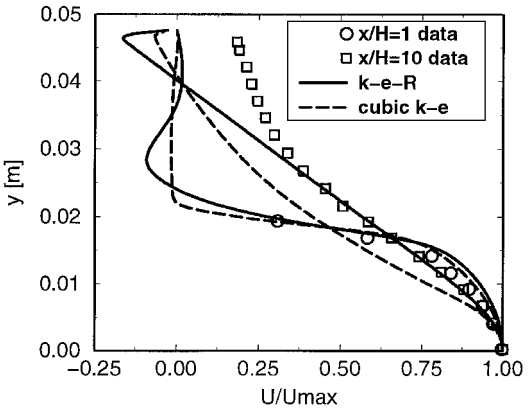

a) Velocity profiles

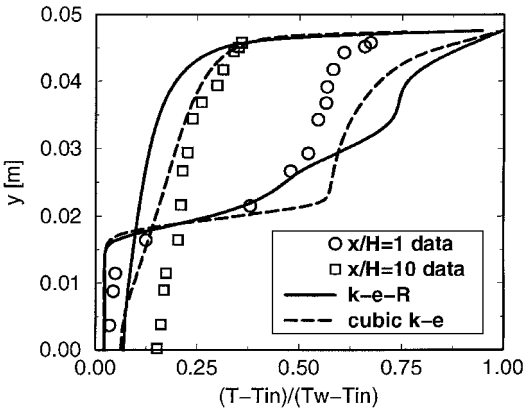

b) Temperature profiles

Fig. 7 Sudden expansion.

An oblique shock, interacting with the boundary layer downstream of the ramp corner, induces flow detachment with subsequent reattachment onto the ramp surface where a large heat transfer peak occurs. Figure 8a shows the geometry and main flow features. The flow conditions are as follows: $M_\infty = 9.22$, $Re_\infty = 0.47 \times 10^6$/cm, $T_0 = 1070$ K, $T_\infty = 64.5$ K, and $T_w = 295$ K. A compressible flow equilibrium 1-mm-thick turbulent boundary layer (wake strength parameter $\Pi = 0.55$) was imposed at the inflow, together with the following profiles for the turbulence variables:

$$k = \left(\frac{\kappa^2}{C_\mu^{\frac{1}{2}}}\right)\left[y\left(\frac{\mathrm{d}U}{\mathrm{d}y}\right)\right]^2, \qquad y^+ \le 11$$

$$k = \max\left\{k_\infty, \left(\frac{\kappa^2}{C_\mu^{\frac{1}{2}}}\right)\left[y\left(\frac{\mathrm{d}U}{\mathrm{d}y}\right)\right]^2\right\}, \qquad y^+ > 11$$

$$\varepsilon = \frac{2\beta k^{\frac{3}{2}}}{y\left(1 - e^{-\beta\phi y^+{}^2}\right)}, \qquad R = \frac{k^2}{\varepsilon}$$

where $\kappa = 0.41$, $\beta = C_\mu^{3/4}/(2\kappa) = 0.2$, $\phi = 0.166$, and, for this flow, $k_\infty = 8 \times 10^{-7} U_\infty^2$. Calculations using constant inflow conditions yielded practically the same results due to the limited extent of upstream influence in this flow case.

The computations were performed on a 250×200 grid with at least 20 cells inside the viscous sublayer, with the first centroidal points away from the wall at $y^+ \approx 0.1$. The grid was clustered in the x direction, too, centered at the ramp corner. A 200×150 grid was also used to ascertain grid independence of the reported fine mesh results.

Figure 8b shows wall pressure distribution as predicted by the two models. Comparison with the experimental data indicates that the pressure profile is slightly better predicted by the k–ε–R model, albeit the peak level is captured with higher fidelity by the cubic closure. Figure 9 shows that the heat transfer is much better predicted

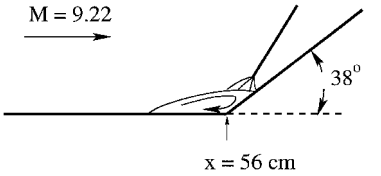

a) Topography and main flow features

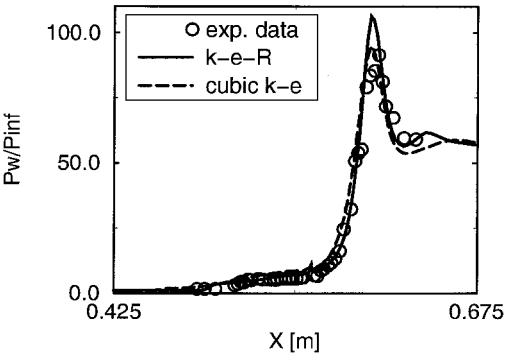

b) Wall pressure; $M = 9.22$

Fig. 8 Hypersonic ramp flow.

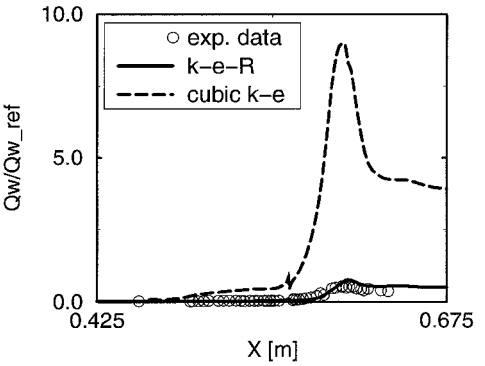

a) Overview

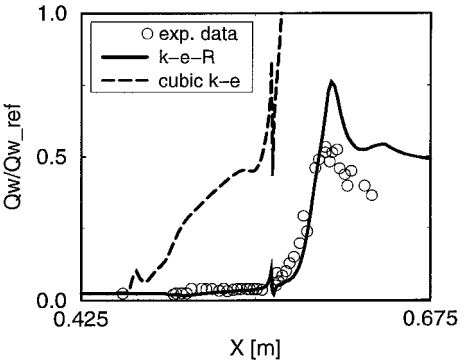

b) Closeup view

Fig. 9 Hypersonic ramp flow, $M = 9.22$; wall heat transfer.

by the three-equation model. That the cubic model captures the pressure distribution while its predicted heat transfer is much too high suggests that, in separated flow regions with simultaneously low mean flow kinetic energy (and, therefore, low strain magnitude) and high-temperature gradients, overpredicted levels of turbulence length scale can lead to rather small errors in the turbulent shear stress and concurrently lead to gross overprediction of the turbulent heat fluxes. Using $\hat{\varepsilon}$ as the destruction of k (rather than ε itself as in k–ε models) avoids excessive levels of turbulence generation in nonequilibrium flow regions (such as recirculation bubbles) as already explained. This results in much improved heat transfer predictions. This effect is seen in Fig. 10, which compares the eddy-viscosity fields predicted by the two models in the separated and reattaching flow regions. The levels predicted by the cubic model

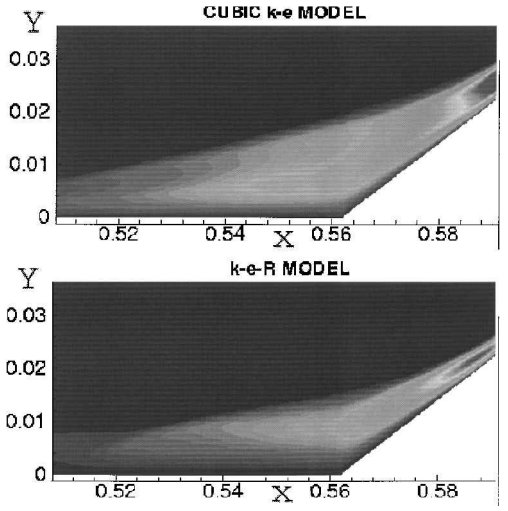

Fig. 10 Hypersonic ramp flow: eddy viscosity levels from the cubic k–ε model and from the k–ε–R closure.

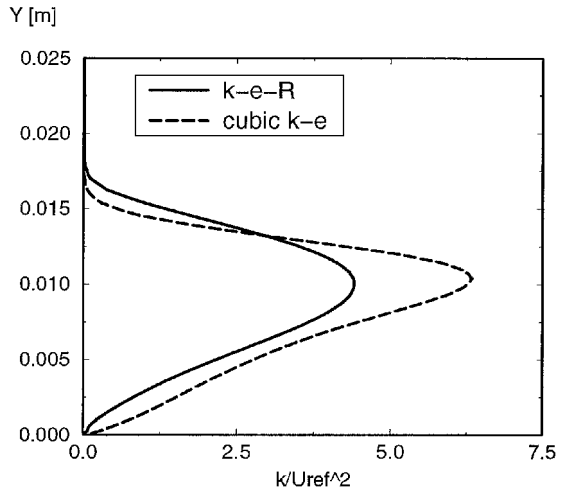

a) Kinetic energy profiles at $x = 0.55$ m

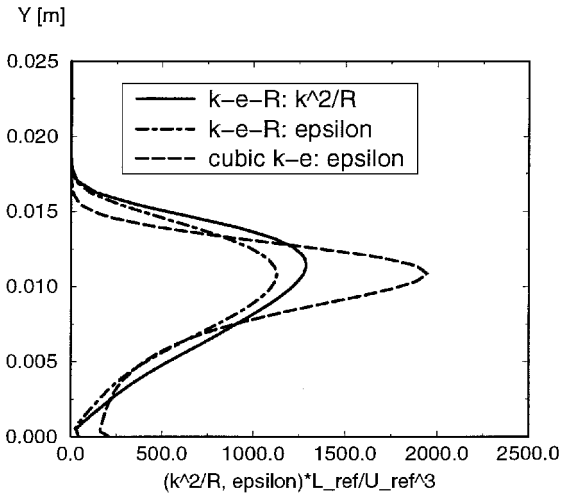

b) Dissipation rate profiles at $x = 0.55$ m; $M = 9.2$

Fig. 11 Hypersonic ramp flow.

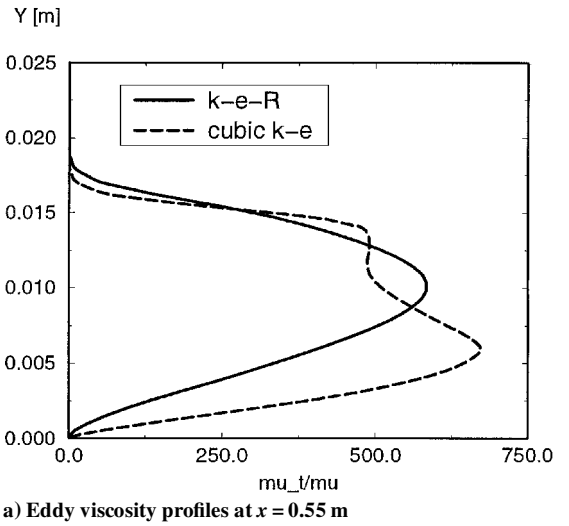

a) Eddy viscosity profiles at $x = 0.55$ m

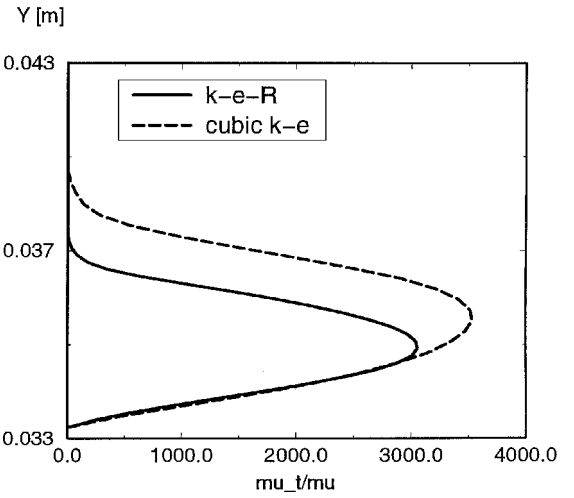

b) Eddy viscosity profiles at $x = 0.60$ m; $M = 9.2$

Fig. 12 Hypersonic ramp flow.

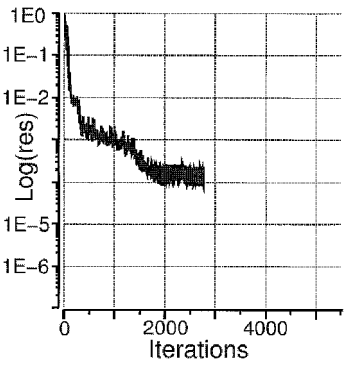

Fig. 13 Hypersonic ramp flow: solution convergence history.

are appreciably higher than those by the three-equation model, especially near the wall. This is also seen in Fig. 11, showing kinetic energy and dissipation rate profiles within the separated flow region ($x = 0.55$ m), and in Fig. 12, where eddy-viscosity profiles at $x = 0.55$ m and in the vicinity of maximum heat transfer at the reattachment location ($x \approx 0.60$ m) are shown. The k profiles (Fig. 11a), indicate that the three-equation model predicts a lower level of turbulence kinetic energy across the entire viscous layer, including a considerably lower peak level than the one predicted by the cubic closure. This translates into less turbulence generation, hence smaller eddy-viscosity levels in the lower half of the shear layer, as seen in Fig. 12a. Application of the dual-dissipation concept has an even more pronounced influence in the reattachment region, as seen in Fig. 12b. The reduced eddy viscosity from the three-equation model prevents overprediction of heat transfer. Figure 11b indicates that, in nonequilibrium flow regions, ε from the k–ε–R closure is much closer to $\hat{\varepsilon}$ than to ε predicted by the cubic model. This is due to the altered k and μ_t levels, the former feeding into the timescale and the latter into the generation term of the ε equation. Last, Fig. 13 shows the convergence history for this calculation,

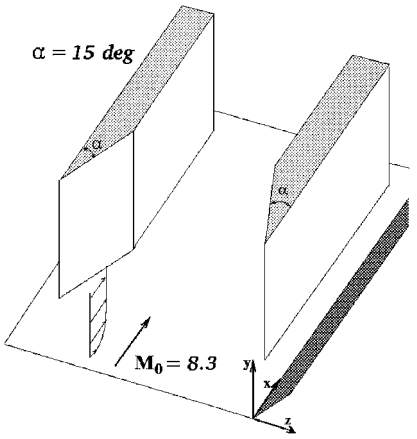

a) Topography

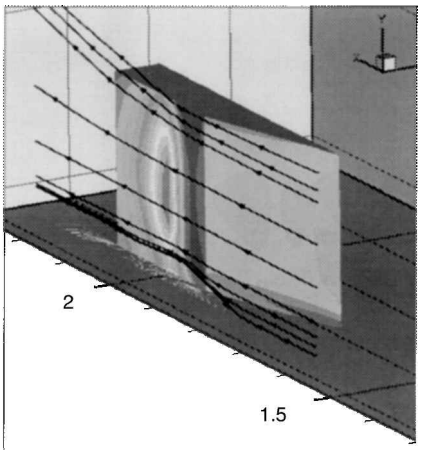

b) Main flow features

Fig. 14 Hypersonic inlet flow.

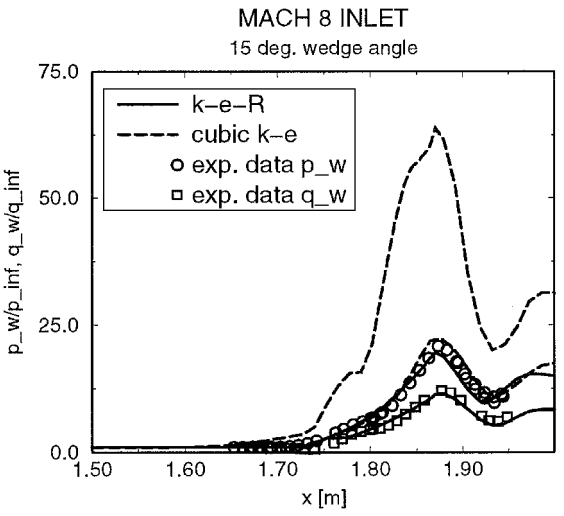

a) Wall pressure and heat transfer along symmetry line

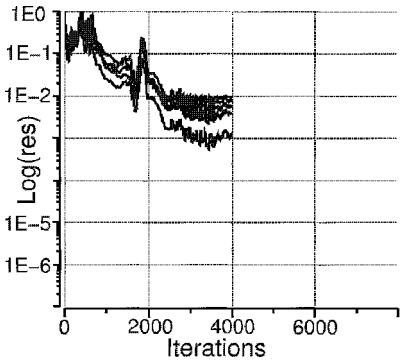

b) Solution convergence history

Fig. 15 Hypersonic inlet flow.

where a residual drop by four orders of magnitude in 2000 steps is seen.

Hypersonic Flow in a Double Wedge Inlet

Kussoy et al.[15] performed extensive experimental measurements on a Mach 8.3 flow in a wedge inlet configuration, with $T_w/T_0 = 0.27$. To predict this complex three-dimensional flowfield, involving crossing shock/boundary-layer interactions, the flow solver was used on a structured mesh consisting of approximately 250,000 cells. First centroidal locations away from walls were at $y^+ \approx 60$ to avoid a much larger grid size. A wall function that accounts for compressibility and heat transfer effects was employed. This wall function uses the van Driest transformed velocity (Ref. 10) in Spalding's law of the wall (Ref. 10) from which the friction velocity, $u_\tau = (\tau/\rho)_w^{1/2}$, is obtained. This is used to determine the momentum and energy wall fluxes:

$$\tau_w = \rho_w u_\tau^2 \tag{21}$$

$$q_w = \tau_w \left[\frac{C_p(T_w - T_1)}{Pr_t U_t} - \frac{U_t}{2} \right] \tag{22}$$

where U_t is the local tangent-to-wall velocity component at the wall-adjacent centroid and T_1 is the temperature there.

Figure 14a shows a sketch of the topography and Fig. 14b is an overview of the flow in the region of the wedges, showing pressure contours on one wedge surface and streamlines. It is observed that the flow in the midregion of the wedge maintains an approximately two-dimensional flavor. The high-pressure region downstream of the shoulder is due to shock impingement from the other wedge. The streamlines at the wall/wedge juncture clearly show streamwise separation due to the adverse pressure gradient downstream of the wedge shoulder. Flow spillage at the upper end of the wedge, due to cross-stream pressure gradient, is also observed. Figure 15a compares predicted wall pressure and heat transfer, along the symmetry line, with corresponding measurements. As in the Mach 9 case, the three-equation model yields very good agreement with both pressure and heat transfer data. The cubic k–ε closure exhibits the same trend observed in the preceding case: very good pressure prediction and large overprediction of heat transfer. The near-wall inadequacy of the ε equation under strong nonequilibrium conditions evidently overwhelms the advantages of this nonlinear model in terms of its otherwise superior physics. Finally, Fig. 15b shows the convergence history plot; two and one-half orders of magnitude drop in flow residuals was obtained in 3000 steps.

Concluding Remarks

This paper demonstrated the feasibility of using a k–ε turbulence closure, based on two dissipation rates, to predict successfully wall heat transfer under high-speed, separated flow conditions. The CFD++ flow solver, in conjunction with a linear three-equation k–ε–R model and a cubic k–ε turbulence closure, was used to predict several flow cases including three involving wall heat transfer. Both closures performed well in pressure distribution predictions, but the three-equation model excelled in predicting heat transfer levels under high-speed, nonequilibrium conditions. The excessive levels of heat transfer predicted by the cubic model (and by most other k–ε closures) suggest that in separated flow regions with simultaneously low mean flow kinetic energy (and, therefore, low strain magnitude) and high temperature gradients, overpredicted levels of the turbulence length scale, while leading to rather small errors in the turbulent shear stress, cause a large overprediction of the turbulent heat fluxes. In contrast, inclusion of the R equation in a linear k–ε model enabled the definition of a second dissipation rate $\hat{\varepsilon}$ applied as the destruction term in the k equation. This term is independent of the

conventional dissipation rate ε in the immediate vicinity of walls. The latter is retained for the determination of the eddy-viscosity field. Application of this dual-dissipation concept led to reduced levels of turbulence generation in nonequilibrium flow regions and enabled the three-equation model to predict correctly heat transfer under high-speed, separated flow conditions. A nonlinear version of this model will be considered in future work.

References

[1]Launder, B. E., "On the Computation of Convective Heat Transfer in Complex Turbulent Flows," *Journal of Heat Transfer*, Vol. 110, Nov. 1988, pp. 1112–1128.

[2]Huang, P. G., Bradshaw, P., and Coakley, T. J., "Turbulence Models for Compressible Boundary Layers," *AIAA Journal*, Vol. 32, No. 4, 1994, pp. 735–740.

[3]Chakravarthy, S., Peroomian, O., and Sekar, B., "Some Internal Flow Applications of a Unified-Grid CFD Methodology," AIAA Paper 96-2926, July 1996.

[4]Peroomian, O., Chakravarthy, S., and Goldberg, U., "A 'Grid-Transparent' Methodology for CFD," AIAA Paper 97-0724, Jan. 1997.

[5]Peroomian, O., Chakravarthy, S., Palaniswamy, S., and Goldberg, U., "Convergence Acceleration for Unified-Grid Formulation Using Preconditioned Implicit Relaxation," AIAA Paper 98-0116, Jan. 1998.

[6]Batten, P., Leschziner, M. A., and Goldberg, U. C., "Average-State Jacobians and Implicit Methods for Compressible Viscous and Turbulent Flows," *Journal of Computational Physics*, Vol. 137, 1997, pp. 38–78.

[7]Goldberg, U. C., "Exploring a Three-Equation R–k–ε Turbulence Model," *Journal of Fluids Engineering*, Vol. 118, No. 4, 1996, pp. 795–799.

[8]Durbin, P. A., "Near-Wall Turbulence Closure Modeling without 'Damping Functions,'" *Theoretical and Computational Fluid Dynamics*, Vol. 3, 1991, pp. 1–13.

[9]Goldberg, U., Batten, P., Palaniswamy, S., Chakravarthy, S., and Peroomian, O., "Hypersonic Flow Predictions Using Linear and Nonlinear Turbulence Closures," *Journal of Aircraft*, Vol. 37, No. 4, 2000, pp. 671–675.

[10]White, F. M., *Viscous Fluid Flow*, 1st ed., McGraw–Hill, New York, 1974.

[11]Spalart, P. R., and Allmaras, S. R., "A One-Equation Turbulence Model for Aerodynamic Flows," AIAA Paper 92-0439, Jan. 1992.

[12]Délery, J. M., "Experimental Investigation of Turbulence Properties in Transonic Shock-Wave/Boundary-Layer Interactions," *AIAA Journal*, Vol. 21, No. 2, 1983, pp. 180–185.

[13]Baughn, J. W., Hoffman, M. A., Launder, B. E., Lee, D., and Yap, C., "Heat Transfer, Temperature, and Velocity Measurements Downstream of an Abrupt Expansion in a Circular Tube at a Uniform Wall Temperature," *Journal of Heat Transfer*, Vol. 111, Nov. 1989, pp. 870–876.

[14]Coleman, G. T., and Stollery, J. L., "Heat Transfer from Hypersonic Turbulent Flow at a Wedge Compression Corner," *Journal of Fluid Mechanics*, Vol. 56, Pt. 4, 1972, pp. 741–752.

[15]Kussoy, M. I., Horstman, K. C., and Horstman, C. C., "Hypersonic Crossing Shock-Wave/Turbulent-Boundary-Layer Interactions," *AIAA Journal*, Vol. 31, No. 12, 1993, pp. 2197–2203.